Influence of Cu Addition on the Microstructure, Mechanical, and Corrosion Properties of Extruded Mg-2%Zn Alloy

M. Lotfpour, M. Emamy, and C. Dehghanian

Effects of different Cu concentrations on the microstructure, mechanical, and corrosion properties of the extruded Mg-2%Zn alloy were studied by the use of x-ray diffraction, optical microscopy, scanning electron microscopy, energy-dispersive spectroscopy, tensile testing, polarization, and electrochemical impedance spectroscopy (EIS) measurements. The hot-extruded Mg-2%Zn comprised an equiaxed grain structure with the average size of about 13 μm. By adding 5 wt.% Cu, the average grain size decreased to 4 μm, due to the grain refinement behavior of Cu addition. Microstructural observations confirmed the existence of the α-Mg matrix, Mg(Zn,Cu), and Mg(Zn,Cu)$_2$ intermetallics. The results obtained from mechanical testing revealed that Cu addition along with applying hot extrusion increased the hardness significantly from 80 HBN, for Cu-free alloy, to 108 HBN for the extruded Mg-2%Zn-5%Cu alloy. By the addition of 0.5 wt.% Cu, the values of ultimate tensile strength (UTS), elongation, and ultimate compressive strength (UCS) changed from about 233 MPa, 16.8%, and 294 MPa to 260 MPa, 21.5%, and 335 MPa, respectively, as optimum levels. However, more Cu addition (i.e., 5 wt.%) decreased UTS, elongation, and UCS values to 242 MPa, 15.9%, and 272 MPa, respectively, by introducing a high volume fraction of the second phase. On the other hand, tensile yield strength and compressive yield strength increased gradually at higher Cu additions from 128 to 105 MPa in the case of the Cu-free extruded alloy to 165 and 156 MPa for the alloy containing 5 wt.% Cu, respectively. The polarization and EIS results indicated that the extrusion process eliminates the protective film from the Mg-2%Zn alloy surface. The Mg-2%Zn alloy exhibited the best anti-corrosion property among the studied alloys, as further Cu addition increased the intermetallic volume fractions and enhanced the corrosion rate, due to the galvanic couple effect.

1. Introduction

The development of Mg alloys with superb mechanical properties and high corrosion resistance is of great importance. The binary Mg-Zn alloy systems are one of the common commercial Mg alloys, owing to their proper mechanical and corrosion properties (Ref 1-4). Apart from biomedical implants, Mg-Zn alloys can also be used in different industrial fields such as automotive and aerospace components. On the one hand, the maximum solid solubility in Mg is 6.2 wt.% at 341 °C which can enhance solid solution strengthening and age-hardening behavior (Ref 2-6). On the other hand, the Zn-containing Mg alloys illustrate appropriate corrosion behavior and biocompatibility properties (Ref 2, 3). Generally, 0-6 wt.% Zn was prevalent in previous research studies with effective results on the mechanical and corrosion properties, while more Zn addition (∼ 7 wt.%) generated the networks of intermetallic phases, which deteriorated the properties (Ref 2, 4). Trace additions of alloying elements have been regarded as one of the most effective ways to enhance both strength and corrosion resistance. Also, heat treatment, hot extrusion, and rolling were common to enhance their properties (Ref 7-9). The addition of various alloying elements such as Gd (Ref 6), Y (Ref 10), Ca (Ref 11), Ce (Ref 10, 11), Zr (Ref 10, 12), and Cu (Ref 13-15) has reported enhancing the mechanical and corrosion properties of the Mg-Zn alloys suitably. Among them, copper is known as a useful element in commercial Mg alloys, due to its low price in comparison with rare earth (RE) elements and its proper effects on the castability, ductility, and age-hardening responses (Ref 13-23). Based on recent studies in the Mg-Zn-Cu alloys, Mg(Zn,Cu) and Mg(Zn,Cu)$_2$ intermetallics were formed with different morphologies in low and high Zn and Cu contents (Ref 13-23). The low volume fraction of Mg(Zn,Cu) intermetallics could properly enhance the UTS and ductility of Mg-Zn-Cu alloys (Ref 18-20). Moreover, it was found that Mg(Zn,Cu) and Mg(Zn,Cu)$_2$ intermetallics affect the creep behavior, while small Mg(Zn,Cu) particles had more positive impacts in comparison with bulk Mg(Zn,Cu)$_2$ intermetallics (Ref 21). Ball et al. (Ref 23) also illustrated that Mg(Zn,Cu)$_2$ intermetallics cannot promote the particle stimulate nucleation (PSN) mechanism for encouraging the dynamic recrystallization during hot extrusion for the ZC71 extruded alloy. Generally, the PSN mechanism occurs if second-phase particles are hard enough and their size is more than 1 μm to be able to form regions known as deformation zones around themselves during deformation (Ref 24). The presence of stress concen-

M. Lotfpour, M. Emamy, and C. Dehghanian, School of Metallurgy and Materials, College of Engineering, University of Tehran, P.O. Box 14395-731, Tehran, Iran. Contact e-mails: mehrablotfpour@yahoo.com, emamy@ut.ac.ir, and cdehghan@ut.ac.ir.

trations and dislocation pileups around the particles can lead to more dynamic recrystallization, grain refinement, and texture weakening (Ref 25).

Furthermore, recent investigations (Ref 26-32) revealed the exceptional potential of Cu-containing Mg alloys in bio-implant applications. Therefore, their corrosion behavior should be paid more attention, while Cu is known as an impurity for the Mg alloys, which can accelerate the corrosion rate, due to the high difference of electrochemical potential between Mg and Mg(Zn,Cu) intermetallics (Ref 27, 28). However, recent studies illustrated that solution heat treatment and hot extrusion could control the corrosion behavior of low Cu-added Mg alloys by lowering the volume fraction of Cu-bearing second phases, introducing homogeneous distribution of intermetallics and grain refinement (Ref 31, 32). Although there have been some researches on the effect of Cu addition on the mechanical and corrosion properties of Mg-2%Zn alloys both in the as-cast state (Ref 13) and T6-extruded condition (Ref 15), no studies have been done on its impact on tensile properties and corrosion behavior of the as-extruded Mg-2%Zn-xCu alloys before applying T6 heat treatment. In condition where Cu intermetallics are expected to be formed uniformly in the refined microstructure of extruded alloys. Therefore, in the present work attention has been concentrated upon Mg-2 wt.%Zn alloy, due to its outstanding corrosion behavior (Ref 4), with the focus on the effect of Cu to unravel the encountered phases, structural evaluations, mechanical properties, and corrosion behavior after applying the hot extrusion process.

2. Experimental Procedure

To fabricate small cylindrical specimens of the Mg-2%Zn-x%Cu alloys (x = 0, 0.1, 0.5, 1, 3, and 5) for extrusion process, Mg was melted by a high-frequency induction furnace at 1023 K. To prevent Mg burning, it was melted in a graphite–ceramic crucible under the protection of 95% CO_2 and 5% SF_6 gas. Then, the calculated additions of Zn and Cu were added to the melt at 1023 K by using the Mg-50%Zn and Mg-20%Cu master alloys. After stirring and stabilizing for 5 min and finally skimming the surface, the melts were cast into a steel mold preheated to 523 K (shown in Fig. 1a).

Furthermore, the inductively coupled plasma spectroscopy (ICP) system was used to analyze the chemical compositions of the cast alloys, as outlined in Table 1.

The Mg-2%Zn cast alloy was homogenized at 588 K for 48 h and then solutionized at 588 K for 5 h followed by water quenching (Ref 17). The Mg-2%Zn-x%Cu alloys were also homogenized and solutionized at 708 K for 48 h and 5 h, respectively, followed by water quenching (Ref 17). Then, the billets required for the extrusion process were prepared by cutting and machining the homogenized pieces into the accurate dimensions (28 mm in length and 29 mm in diameter). By preheating the billets at 573 K for 1 h in an electrical resistance furnace, the extrusion process was applied at the RAM speed of 1 mm/s and the ratio of 12:1. Table 2 lists more information about experimental procedures.

After etching the polished specimens in the acetic picral solution (5 mL acetic acid + 6 g picric acid + 10 mL H_2O + 100 mL ethanol) (Ref 21), the optical microscopy (OM) and scanning electron microscopy (SEM) performed in Vega©Tescan microscope equipped with energy-dispersive spectroscopy (EDS) system were used for the microstructure characterizations. Furthermore, Philips binary x-ray diffraction (XRD) with the Cu-kα radiation was employed for the phase identification.

The Brinell hardness tests were performed from perpendicular cross section to the extruded direction, with the load of 500 Kgf (4903.325 N), the ball diameter of 10 mm, and holding time of 15 s. Also, after machining the extruded rods to the proper dimensions (D = 8 mm, h = 12 mm), the compression tests were carried out by using the mica plates. Moreover, the tensile samples were machined from extruded rods based on the ASTM: E8/E8M-16a standard (Fig. 1b). Compression and tensile tests were performed by the SANTAM STM-20 computerized testing device at the constant crosshead speed of 0.1 mm/min at room temperature. For each alloy, two compression and two tensile samples were prepared and tested. For the tensile test specimens, the fracture surfaces were observed by the SEM.

After machining the samples to the exact surface area of 100 mm^2, the working electrodes were prepared for the polarization and electrochemical impedance spectroscopy (EIS) tests in 3.5 wt.% NaCl solution. For the cell system, two other electrodes were the platinum plate anode and the standard calomel. After immersing the samples for 300 s to reach the stable condition, the EIS tests were carried out initially by changing the frequency from 100 kHz to 0.1 Hz with the voltage step of 0.1 mV. Then, the polarization tests were performed by increasing the potential from − 200 mV in an open-circuit potential (OCP) with the rate of 1 mV/s to the potential of + 200 mV and the current density of 10 mA/cm^2. After that, the corroded surfaces after the polarization tests were
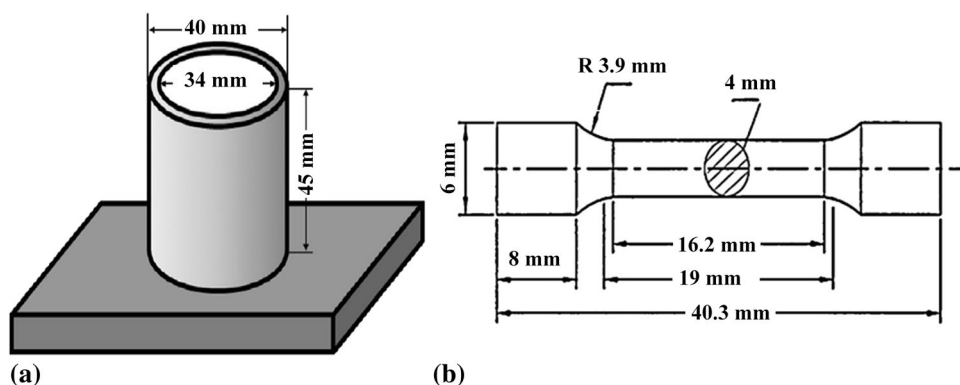
Fig. 1 (a) Schematic of the simple cast iron mold and (b) sketch map of tensile samples

Table 1 Chemical compositions of cast alloys

Alloy, wt.%	Zn	Cu	Mg
Mg-2%Zn	2.43	…	Bal.
Mg-2%Zn-0.1%Cu	1.84	0.15	Bal.
Mg-2%Zn-0.5%Cu	1.93	0.41	Bal.
Mg-2%Zn-1.0%Cu	1.96	0.84	Bal.
Mg-2%Zn-3.0%Cu	2.03	2.89	Bal.

Table 2 Details on sample preparation procedure

Sample preparation procedure	
Casting the Mg-2%Zn-0, 0.1, 0.5, 1, 3, and 5 wt.% Cu	
Heat treatment	
Cu-free Mg-2%Zn alloy	Cu-containing Mg-2%Zn alloys
Homogenized at 588 K for 48 h	Homogenized at 708 K for 48 h
Solutionized at 588 K for 5 h	Solutionized at 708 K for 5 h
Extrusion	
Preheating at 573 K for 1 h	
Extrusion at the RAM speed of 1 mm/s and the ratio of 12:1	

washed with 180 g/L chromic acid and characterized with the SEM microscopy. The corrosion current density (I_{corr}) and corrosion potential (E_{corr}) were calculated by extrapolating the polarization curves. Moreover, the ZView software was used for fitting the equivalent circuit of the EIS tests.

3. Results and Discussion

3.1 Microstructure Characterization

Figure 2 presents the OM and related SEM micrographs of the extruded Mg-2%Zn alloys with different Cu contents. Figure 3 also shows the variation of grain size and volume fraction of Cu-containing second phases for the above alloys.

As depicted in Fig. 2, the microstructures of the extruded alloys include the equiaxed grains and some bright particles (shown by red arrows), which are distributed along the extrusion direction. These bright intermetallics may be the same particles that were formed as a semi-continuous network in the as-cast alloys (Ref 15, 20). After hot extrusion, these particles were fractured and allocated along the extrusion direction (Fig. 2f) (Ref 20, 23). Moreover, the average size of the grains for the base alloy is about 13 μm, which reduces to 9 μm by the addition of 0.1 wt.% Cu, and when 5 wt.% Cu is added, it increases to 4 μm (Fig. 3). From Fig. 3, it can be seen that the volume fraction of second phases for the Cu-free alloy is approximately below 0.1% and increases to more than 16% by the addition of 5 wt.% Cu, resulted in the introduction of more bright secondary phase precipitates (as shown in Fig. 2).

The second-phase particles could have a remarkable influence on the texture, recrystallization behavior, and mechanical properties during hot deformation (Ref 24). Humphreys and Hatherly explained the notable effects of second-phase particles on the microstructural evolution during mechanical processing

as (1) finer grain size by increasing the driving force for recrystallization, (2) acting as nucleation sites, and (3) having the pinning effect during grain growth (Ref 24). Therefore, the final grain size is mainly dependent on the particle size and its interparticle spacing. Robson et al. (Ref 33) manifested that large particles (> 1 μm diameter) could form the deformation zones with a misorientation gradient around them, where PSN could occur there. In the present study, the size of the Cu-containing intermetallics is more than 1 μm, illustrating the potent effect of intermetallics on the development of the PSN mechanism. However, Ball et al. (Ref 23) explained the inability of Mg-Zn-Cu-containing intermetallics in promoting the PSN mechanism, due to non-correlation of the grain size distribution with the distribution of intermetallics. The grain size was large, and the allocation of intermetallics was wide (Ref 23). In this study, the volume fraction of intermetallic phases in the microstructure is increased by adding more Cu content, the intermetallics of which, in comparison with the Ball et al. (Ref 23) research study, are distributed more extensively around the microstructure. As expected, the Mg-2%Zn-3%Cu and Mg-2%Zn-5%Cu alloys have much more intermetallics than that of the ZC71 alloy. With the use of more Cu contents, the PSN mechanism and Zenner pinning effect (blocking the grain boundaries during deformation) could be two main factors for grain refinement of the alloys and promotion of the dynamic recrystallization during the extrusion process.

To unravel the formed phases in different alloys, Mg_xZn_y, $Mg(Zn,Cu)$, and $Mg(Zn,Cu)_2$ intermetallics have been discovered in some research studies (Ref 13-23). Jun et al. (Ref 22) reported that Cu and Zn atoms could incorporate into Mg-Zn and Mg-Cu eutectic phases to form $Mg(ZnCu)$ and $Mg(Zn,Cu)_2$ phases instead of $MgZn$, $MgZn_2$, and $MgCu_2$ intermetallics. Therefore, the main intermetallics in the current study are high probably the $Mg(Zn,Cu)$ and $Mg(Zn,Cu)_2$ phases. Further investigation was necessary to confirm the presence of such intermetallics in the current work. In this regard, XRD patterns of the extruded Mg-2%Zn-containing Cu (presented in Fig. 4) revealed that in Mg-2%Zn-1%Cu alloy, $Mg(Zn,Cu)$ phase is detected as the main intermetallic, whereas in the extruded Mg-2%Zn alloy with 5 wt.% Cu, $Mg(Zn,Cu)_2$ intermetallic is detected alongside with $Mg(Zn,Cu)$ as the major phases. The same XRD results were observed in the previous research study for the cast alloys (Ref 13), in which at low Cu concentrations (i.e., 0.1, 0.5, and 1 wt.%), more $Mg(Zn,Cu)$ with less $Mg(Zn,Cu)_2$ intermetallics were seen, but with high Cu contents (i.e., 3 and 5 wt.%), the $Mg(Zn,Cu)_2$ phase was found to be dominant.

Figure 5 shows the SEM micrograph and related EDS analysis of the extruded Mg-2%Zn-x%Cu (x = 0, 1, and 5) alloys.

As depicted in the Mg-Zn phase diagram (Ref 34), the Mg-2%Zn binary alloy must contain a low volume fraction of intermetallics (Fig. 5a). The corresponding EDS results of two points of the extruded Mg-2%Zn alloy have also been tabulated below the figure. The points A and B display two white particles that are located at the grain boundaries. These particles contain Mg and Zn elements; however, their chemical compositions cannot be determined precisely because their small size generates major measurement errors. The same results have been reported in another research (Ref 4), in which some bright particles were seen at the grain boundaries of the Mg-Zn alloys with 2-5 wt.% Zn additions that could not be discovered by the
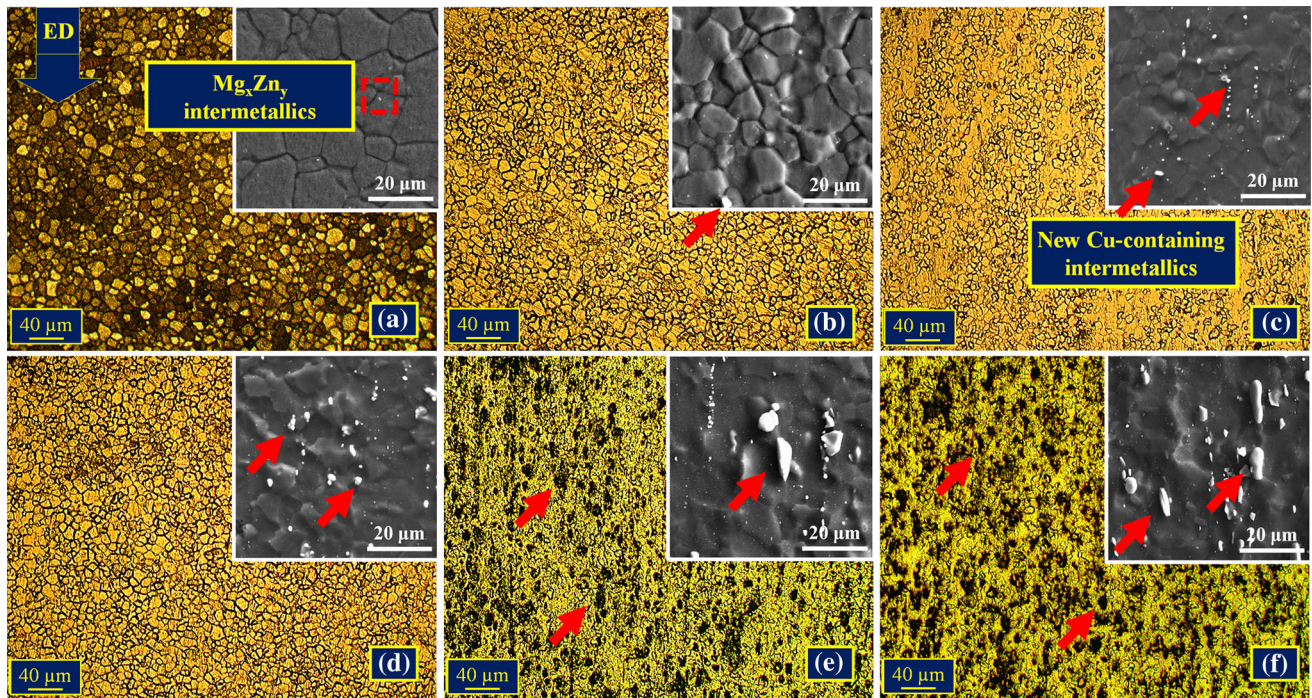
Fig. 2 Optical and related SEM micrographs of the extruded Mg-2%Zn alloy with: (a) 0, (b) 0.1, (c) 0.5, (d) 1, (e) 3, and (f) 5 wt.% Cu additions (Color figure online)
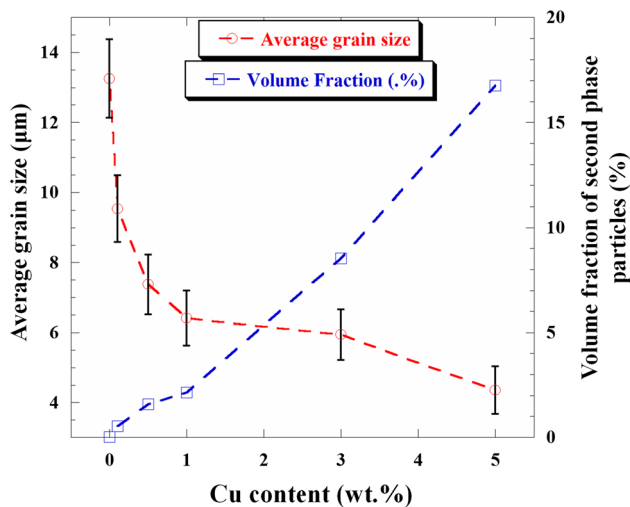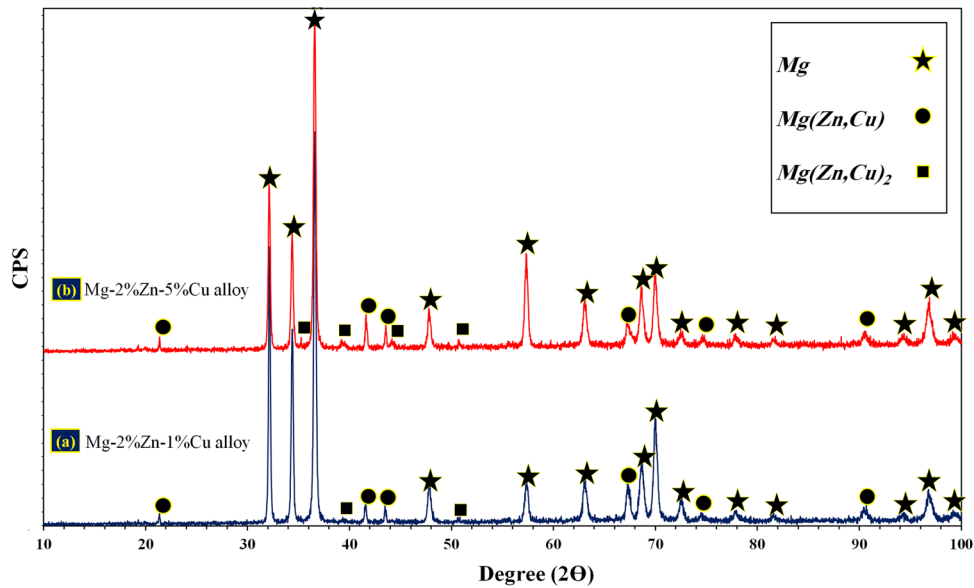

Fig. 3 Variation of the average grain size and the volume fraction of second-phase particles of the extruded Mg-2%Zn alloy with different Cu contents

XRD analysis. On the other hand, due to their low volume fraction and also small size, their chemical compositions could not be determined exactly by the EDS analysis and were introduced as Mg_xZn_y (Ref 4). Moreover, Cai et al. (Ref 2) worked on the Mg-1%Zn, Mg-5%Zn, and Mg-7%Zn alloys and found that the MgZn intermetallics were detected only for the cast Mg-5%Zn and Mg-7%Zn alloys (Ref 2). Therefore, according to these two research studies and also the Mg-Zn phase diagram, it is reasonable that XRD analysis cannot detect any Mg-Zn-containing intermetallics for the Mg-2%Zn alloy. Also, based on the Song et al. study, the white particles in
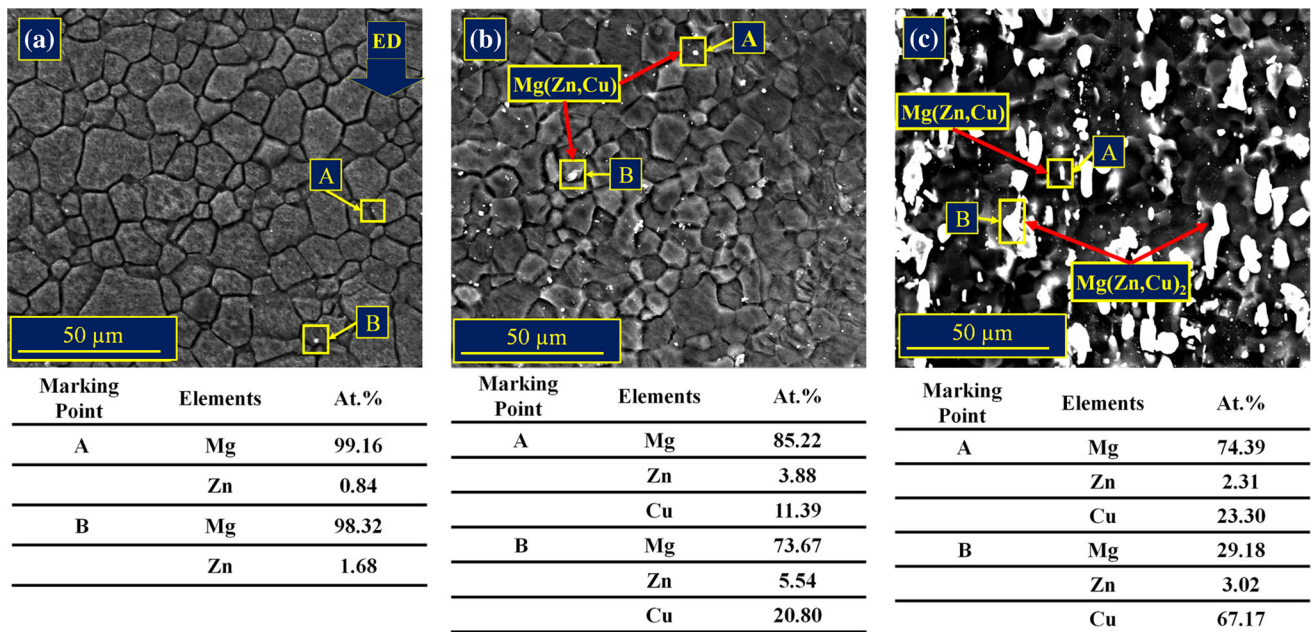
Fig. 5a can be named as Mg_xZn_y intermetallic (Ref 4). By adding 1 wt.% Cu, there are some bright particles (marked with A and B) that display the average composition of $Mg_{75}Cu_{20}Zn_5$, corresponding to Mg(Zn,Cu) compound. As discussed before, Cu atoms can incorporate MgZn intermetallics and form the Mg(Zn,Cu) second-phase particles (Ref 22). Besides, with more Cu contents, the $MgCu_2$ intermetallic is formed, which is a Laves phase similar to the $MgZn_2$ intermetallics (Ref 35). As mentioned earlier, the Cu and Zn atoms also can dissolve in $MgZn_2$ and $MgCu_2$ intermetallics and form the $Mg(Zn,Cu)_2$ second-phase particles (Ref 22).

As illustrated in Fig. 5c, the microstructure of the extruded Mg-2%Zn-5%Cu alloy consists of two forms of intermetallics, bulky particles with an irregular shape, marked as A, and small bright particles, marked as B. Similar to their morphologies, Cu and Zn contents for these two different points are not the same. The qualitative analysis of A and B points is $Mg_{75}Cu_{23}Zn_2$ and $Mg_{30}Cu_{65}Zn_5$, which are analogous to Mg(Zn,Cu) and $Mg(Cu,Zn)_2$ compounds, respectively. Figure 6 depicts further results of structural analysis by elemental mapping and line EDX spectra, clarifying the presence of two different morphologies of the Cu-containing intermetallics.

As shown in Fig. 6a, the Mg(Zn,Cu) intermetallics can be observed with smaller dimension and brighter color in comparison with the $Mg(Zn,Cu)_2$ compounds, due to its lower copper contents. In Fig. 6b, it can also be seen that the larger particles that have more Cu contents can be related to the $Mg(Zn,Cu)_2$ intermetallics. Moreover, Golmakaniyoon et al. (Ref 21) also showed that $Mg(Zn,Cu)_2$ intermetallic is formed in lamellar eutectic structure, but Mg(Zn,Cu) intermetallic is observed in the form of small particles in the as-cast condition. During the extrusion process, both bulky and small particles

Fig. 4 XRD patterns for the extruded Mg-2%Zn alloy, with different Cu addition, (a) 1 wt.%, (b) 5 wt.%

Marking Point	Elements	At.%
A	Mg	99.16
	Zn	0.84
B	Mg	98.32
	Zn	1.68

Marking Point	Elements	At.%
A	Mg	85.22
	Zn	3.88
	Cu	11.39
B	Mg	73.67
	Zn	5.54
	Cu	20.80

Marking Point	Elements	At.%
A	Mg	74.39
	Zn	2.31
	Cu	23.30
B	Mg	29.18
	Zn	3.02
	Cu	67.17

Fig. 5 SEM micrograph with related EDS analysis for the extruded (a) Mg-2%Zn, (b) Mg-2%Zn-1%Cu, and (c) Mg-2%Zn-5%Cu alloy

were broken and distributed along the extrusion direction, identical with particles observed in Fig. 5 and 6.

3.2 Mechanical Properties

Mechanical properties of the extruded Mg-Zn-Cu alloys have been evaluated with tensile, compression tests, and Brinell hardness measurements which are summarized in Table 3.

Figure 7 illustrates the variation of hardness as a function of different Cu content for the extruded Mg-2%Zn-x%Cu alloys. The Brinell hardness of the Cu-free alloy is 80 HBN, which reaches 108 HBN with the addition of 5 wt.% Cu. In comparison with the as-cast condition of the same alloy (Ref 13), an improvement in hardness has been achieved after hot extrusion. This improvement can be related to the obtained fine

grain structure, which culminates in the work hardening of the material, and Cu addition, which causes the formation of more intermetallics.

Figure 8 depicts the typical engineering stress–strain curves of the extruded Mg-2%Zn alloys with different Cu additions. To illustrate the impact of Cu addition on the tensile properties of the extruded alloys, the comparison among the UTS, elongation, and YTS values is shown in Fig. 9.

According to Fig. 9 and Table 3, the UTS and elongation values enhance from about 233 MPa and 16.8% to their optimum levels, 260 MPa and 21.5%, respectively, in the alloy containing 0.5 wt.% Cu addition. However, by more Cu additions (i.e., 5 wt.%), the UTS and elongation values decrease to 242 MPa and 15.9%, respectively. The improve-
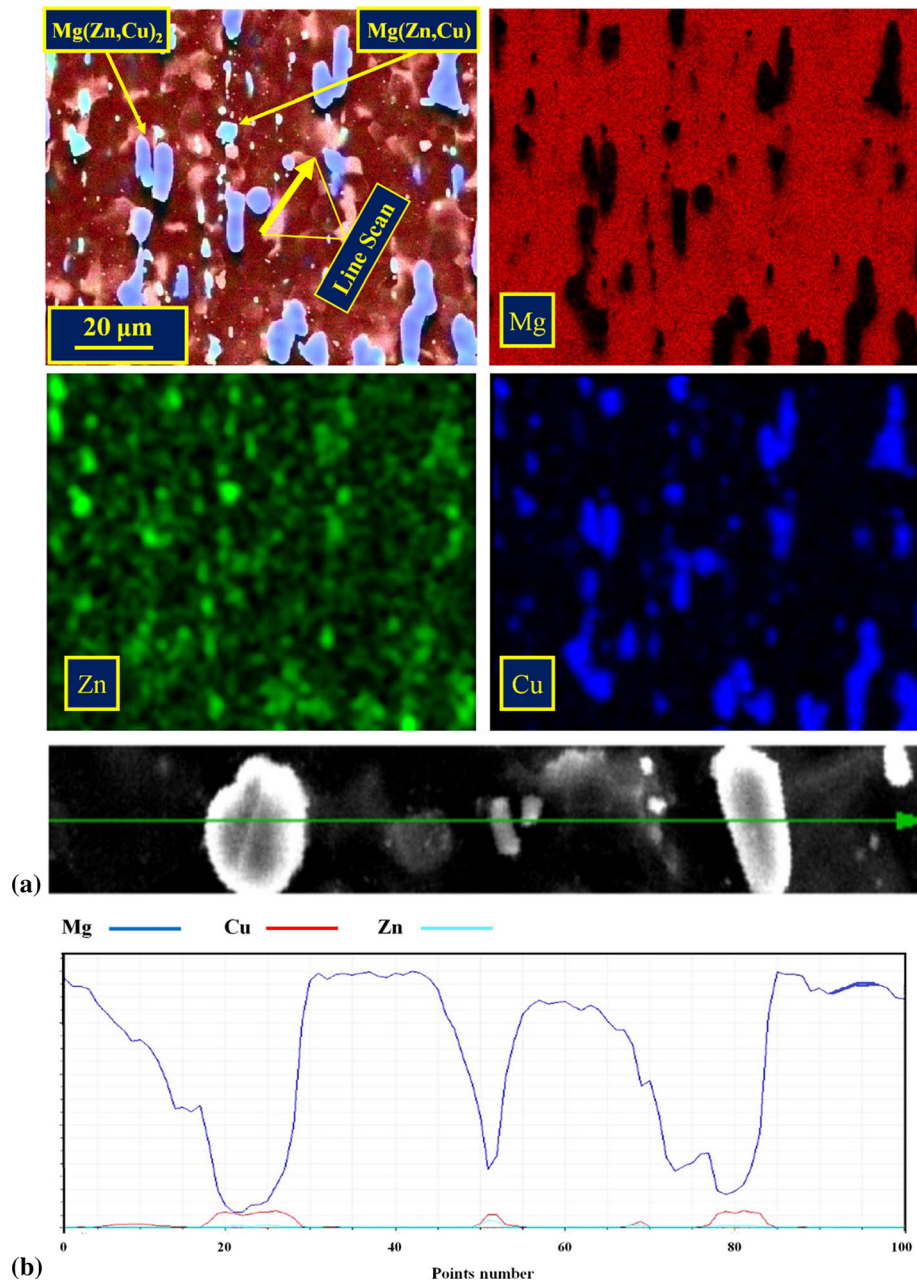
Fig. 6 (a) Element mapping images, (b) line scanning EDS analysis of the extruded Mg-2%Zn-5%Cu alloy

ment in tensile properties of the extruded alloys in comparison with the cast alloys can be achieved by positive influences of hot extrusion process in eliminating the casting defects, the formation of the nearly equiaxed grain structure, breaking the continuous networks of intermetallics, and decreasing the volume fraction of intermetallics because of dissolving in the matrix during solutionizing heat treatment (Ref 13, 15). However, the adverse trend of the UTS and elongation after 0.5 wt.% Cu content occurs, due to the volume fraction enhancement of the coarse and brittle intermetallics encouraging the initiation of cracks. These data explain the unfavorable effects of the Cu-rich intermetallics on the mechanical properties, which have also been discussed in recent research (Ref 20). On the other hand, more Cu additions up to 5 wt.% are led to a significant increment in the YTS from 128 to 165 MPa. Enhancement of the YTS can be the result of the increase in the

volume fraction of intermetallics with higher Cu additions, which can prevent the dislocations motion and improve the YTS (Ref 36).

Moreover, the YTS improves not only because of the volume fraction of the second phase but also as a result of grain boundary strengthening, which can be discussed based on the well-known Hall–Petch equation:

$$\sigma = \sigma_0 + kd^{-1/2} \qquad \text{(Eq 1)}$$

where σ_0 is the frictional stress, k is the Hall–Petch coefficient, and d is the grain size (Ref 37, 38). According to Fig. 2, 3, and 9, the YTS values of the extruded Mg-2%Zn-x%Cu alloys rely on the grain size (Fig. 3 and 9). Moreover, the Hall–Petch relationship is extracted by plotting the YS via the inverse square root of grain size (shown in Fig. 10). The H–P equation

Table 3   Results of compression tests and Brinell hardness measurements

Alloy	Ultimate tensile strength (UTS), MPa	Tensile elongation (%)	Yield tensile strength (YTS), MPa	Brinell hardness (HB)	Ultimate compressive strength (UCS), MPa	Yield compressive strength (YCS), MPa	Yield asymmetry ratio
Mg-2%Zn	233 ± 6	16.8 ± 2.2	128 ± 3	80 ± 3	294 ± 6	105 ± 3	0.82
Mg-2%Zn-0.1%Cu	251 ± 7	19.6 ± 2.4	133 ± 2	91 ± 5	327 ± 7	113 ± 1	0.84
Mg-2%Zn-0.5%Cu	260 ± 5	21.5 ± 1.9	134 ± 2	102 ± 3	335 ± 6	119 ± 1	0.88
Mg-2%Zn-1%Cu	253 ± 6	18.1 ± 1.5	141 ± 5	103 ± 5	309 ± 6	125 ± 2	0.89
Mg-2%Zn-3%Cu	248 ± 7	17.2 ± 1.6	149 ± 3	106 ± 2	286 ± 8	138 ± 6	0.92
Mg-2%Zn-5%Cu	242 ± 6	15.9 ± 2.3	165 ± 3	108 ± 3	272 ± 7	156 ± 3	0.94
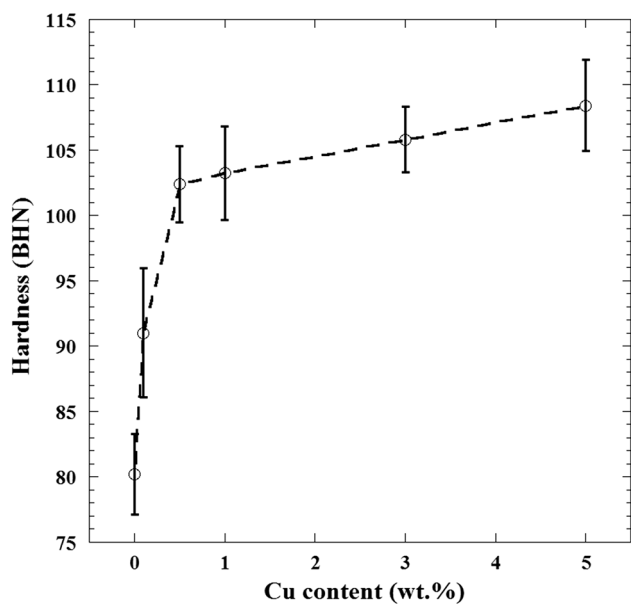
Fig. 7 Brinell hardness of the extruded Mg-2%Zn alloy as a function of Cu concentration

is $\sigma = \sigma_0 + \frac{k}{\sqrt{D}}$ ($\sigma = 74.78 + \frac{178.32}{\sqrt{D}}$), and its parameters are $k = 178.32$ MPa/μm$^{1/2}$ and $\sigma_0 = 74.78$. The relative figure indicates that the grain size is a significant term to control the mechanical properties. However, the scattered values are associated with the solid solution strengthening and particle hardening effects of Zn and Cu additions. The k value is nearly consistent with that of the Mg-5.1Zn alloy in another study, which was 217 MPa/μm$^{1/2}$ (Ref 39).

Figure 11 demonstrates the SEM images of tensile fracture surfaces of the extruded Mg-Zn-Cu alloys.

The Cu-free Mg-2%Zn alloy is characterized by few cleavage planes, tearing ridges, and some plastic dimples. The fracture surface of the alloy is partly quasi-cleavage with the ductile mode of fracture in some regions (Fig. 11a). With 0.5 wt.% Cu addition, the fracture surface is observed with more fine dimples in comparison with the extruded Mg-2%Zn alloy. Therefore, for the extruded Mg-2%Zn-0.5%Cu alloy, the ductile mode of fracture is dominant. Generally, the ductility of the alloys including intermetallic compounds is characterized by the presence of particles at the bottom of the dimples. If the particles are hard enough during tensile testing, strong bonding at the interface exists between the particle and the matrix. Thus, these hard particles can transfer the load from the matrix to the particles resulting in ductility improvement in the ductility of the material (Ref 20). By adding higher Cu contents (i.e., ≥

1 wt.%), broken Cu-containing intermetallics can be seen obviously at the bottom of the dimples, which can exhibit the deterioration effects of the Cu-containing intermetallics on ductility. However, the figures can fully assure the fact that although elongation of the alloys drops at higher Cu additions, the extruded alloys mainly show the domination of ductile mode of fracture, as it can also be observed in Fig. 9 that the elongation values of all the hot-extruded alloys are above 15%.

Figure 12 displays the curves of compressive strength via strain. Furthermore, Fig. 13 shows the TYS, CYS, and also YAR values as a function of Cu concentrations.

The CYS value enhances gradually with further Cu additions from 105 to 156 MPa. Also, the YAR value improves from 0.82 to 0.94 with higher copper addition (up to 5 wt.%). Generally, when the extruded Mg alloys are subjected to the tensile and compression testing parallel to the extrusion direction, the CYS is lower than the TYS value (Ref 40). In the Mg alloys, at the yield point, the principal mechanism for initiating the plastic deformation is the activation of the $\{10\,\bar{1}2\}$ twinning or the second-order pyramidal $\langle c + a \rangle$ slip (Ref 40). At ambient temperature, the critical resolved shear stress (CRSS) or Schmid factor of the $\langle c + a \rangle$ slip is higher than that for the $\{10\,\bar{1}2\}$ twinning, which eases the occurrence of $\{10\,\bar{1}2\}$ twinning during the compression test (Ref 40). This is the main reason which accounts for the difference between the TYS and CYS values known as yield asymmetry. Generally, the YAR value changes by grain size, texture, the volume fraction of second-phase particles, load direction, extrusion ratio, and temperature, because these factors can affect the twinning rate in the compression test (Ref 36, 40-43). In the present study, variables are grain size and volume fraction of the intermetallics. By increasing the Cu contents, finer grain size and higher volume fraction of second phases are achieved, which harden the activation of the $\{10\,\bar{1}2\}$ plane twinning and enhance the CYS and YAR values.

3.3 Corrosion Resistance

The corrosion resistance of the extruded alloys has been characterized by polarization, EIS tests, and surface appearances. Figure 14 shows the polarization curves stemmed from suspending the alloys in 3.5% NaCl solution. By considering the Tafel extrapolation, E_{corr} and I_{corr} have been calculated directly from the polarization curves and listed in Table 4.

According to Table 4, an increase in I_{corr} of the extruded Mg-2%Zn-x%Cu alloys is in the following order: Mg-2%Zn-0.1%Cu ≈ Mg-2%Zn, Mg-2%Zn-1%Cu, and Mg-2%Zn-5%Cu. The difference between I_{corr} of the extruded Mg-2%Zn and Mg-2%Zn-0.1%Cu is denoted as marginal. Considering the same cathodic potential (marked by the solid blue line

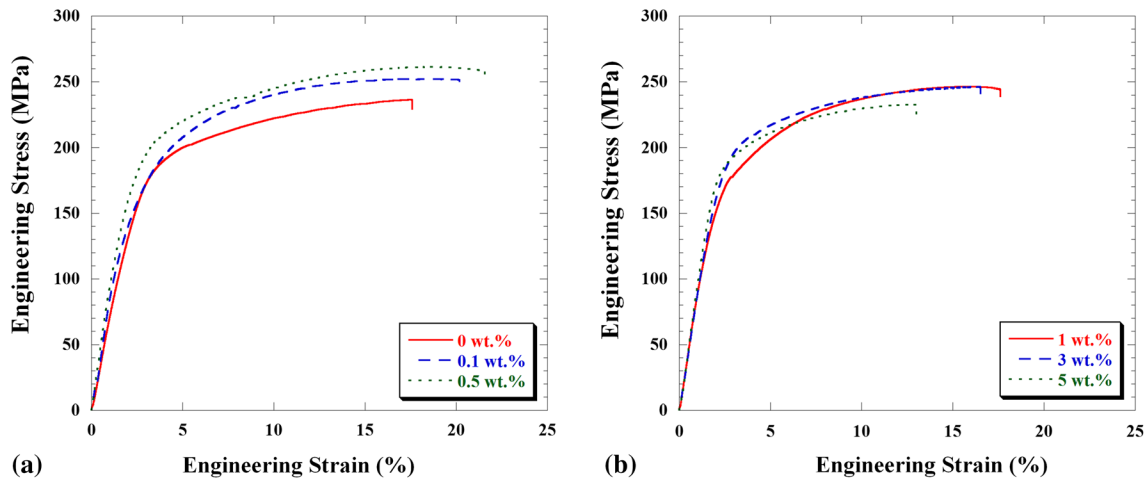**Fig. 8** Engineering stress vs. engineering elongation percentage of the extruded Mg-2%Zn with (a) 0, 0.1, 0.5 and (b) 1, 3, and 5 wt.% Cu additions
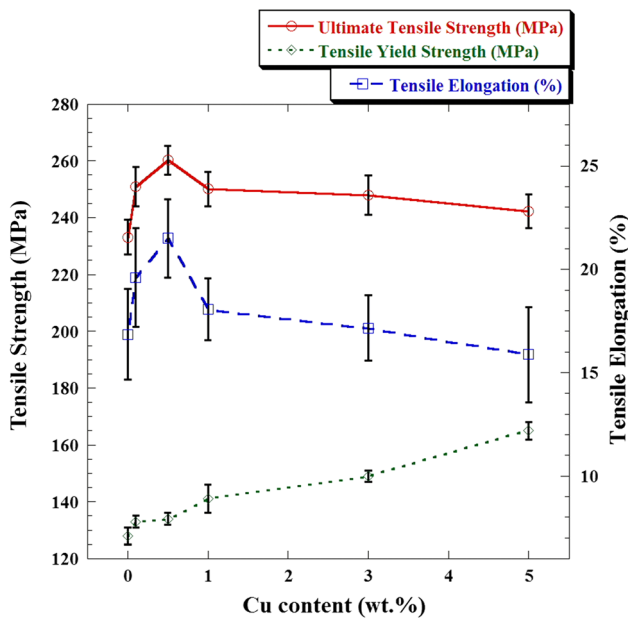

Fig. 9 Variation of the UTS, YTS and Tensile Elongation percentage as a function of Cu concentration

Fig. 10 Variation of the YTS via the inverse square root of grain size, according to the Hall–Petch relationship

in Fig. 14) at the cathodic region of polarization curves, the corrosion current density of the extruded Mg-2%Zn-1%Cu and Mg-2%Zn-5%Cu alloys is the highest, whereas the extruded Mg-2%Zn alloy shows the lowest value. These results are obtained because the corrosion current density is pertinent to the volume fraction of the second phase. The higher the volume fraction is, the weaker the corrosion resistance becomes (Ref 4). Also, in anodic sides of polarization curves, pitting potential (E_p) is an important parameter that happens when a sudden increase in corrosion current prevails as a result of localized corrosion (Ref 2, 4). However, pitting potential is not observed in the anodic curves of the ongoing extruded alloys.

EIS measurements for the extruded Mg-2%Zn-x%Cu alloys have been reported at open-circuit potential (E_{ocp}) as illustrated in Fig. 15.
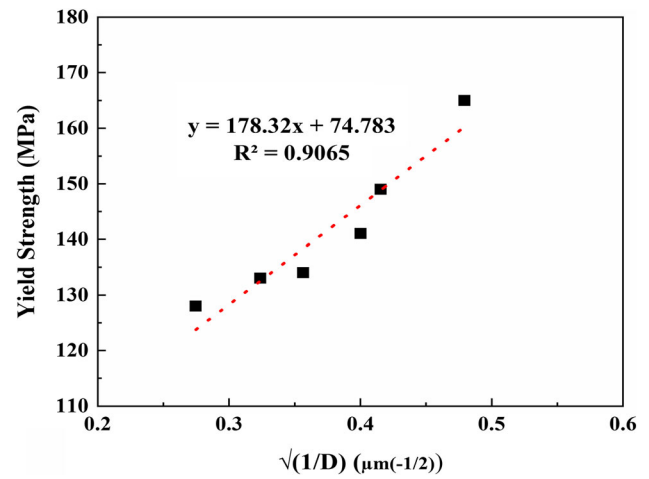
Figure 15a indicates the Nyquist plots, and Fig. 15b and c designates the Bode plots of |Z| and phase angle versus frequency. The latter two figures have been brought to prove the results of Fig. 15a. For comparison between EIS results and clarification of the corrosion mechanisms and rates, the shape and diameter of the loops have been scrutinized (Ref 2). The impedance diagram of the four alloys is characterized by one well-defined capacitive circuit (Fig. 15a). Moreover, the diameter of inductance loops for the extruded Mg-2%Zn alloy is larger than that of the other extruded Cu-bearing alloys. The larger diameter of the inductance loop exhibits better corrosion resistance (Ref 2, 4). The diameter decreases in ascending order as the extruded Mg-2%Zn, Mg-2%Zn-0.1%Cu, Mg-2%Zn-1%Cu, and Mg-2%Zn-5%Cu alloys.

Fitting results of the Nyquist plots of the extruded Mg-2%Zn alloys with different additions of copper are given in Table 5.

R_s represents the solution resistance. R_{ct}, which has been calculated as intersections of capacitance loops with Z'-axis, shows the charge transfer resistance and is a factor for comparing corrosion resistance. C also relates to the electric
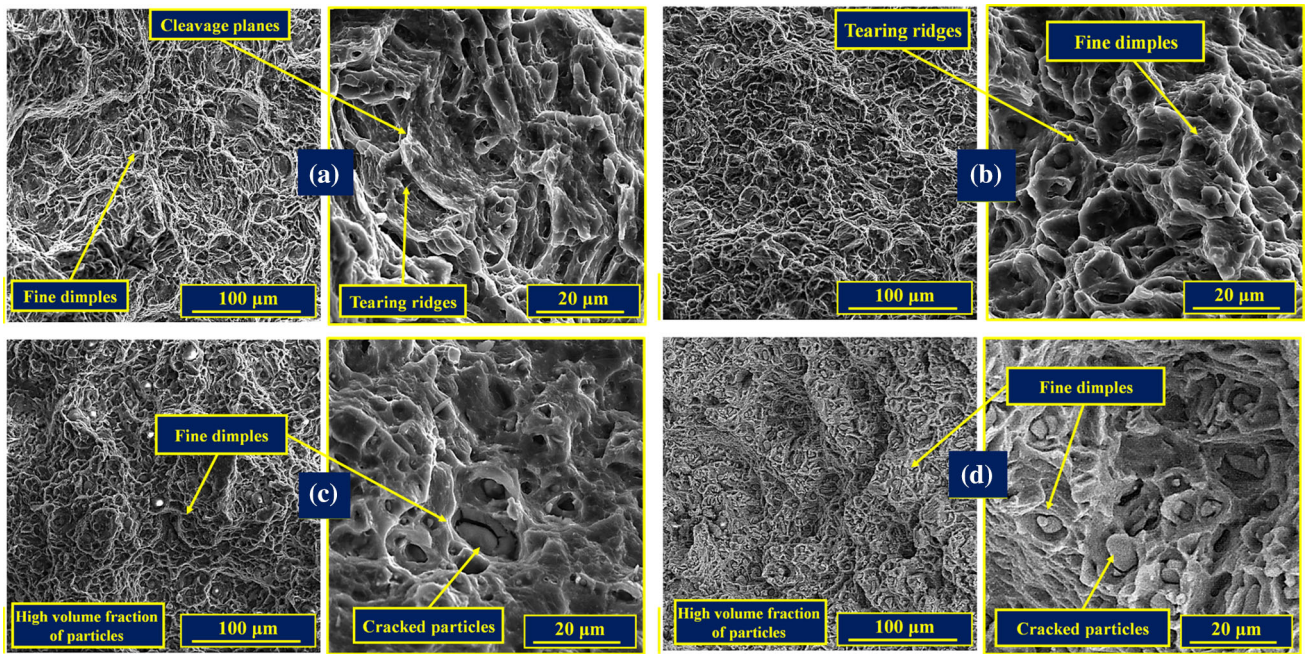
Fig. 11 Fracture surface (SEM micrographs) of the extruded Mg-2%Zn alloy with different Cu additions: (a) 0 wt.%, (b) 0.5 wt.%, (c) 1 wt.%, and (d) 5 wt.%
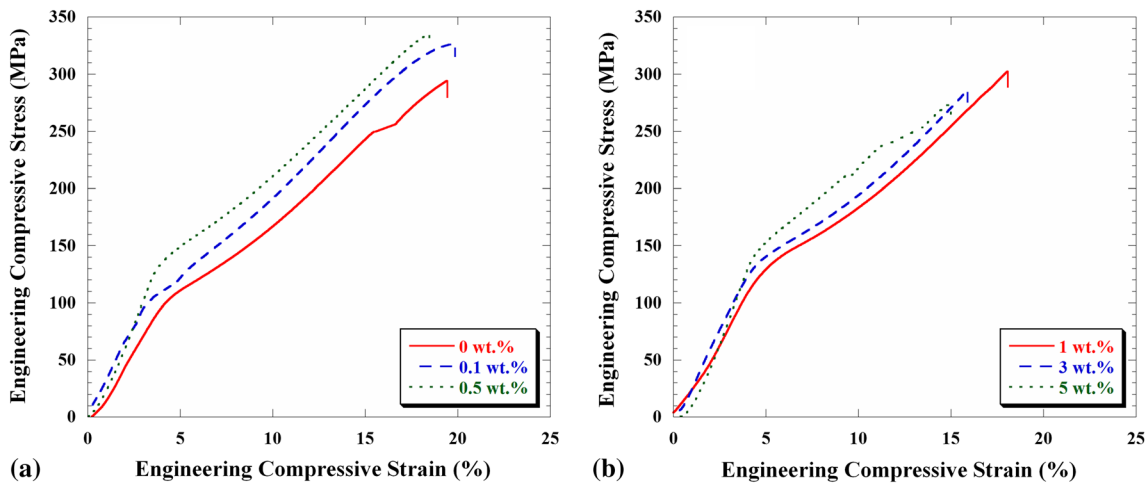

Fig. 12 Engineering compressive stress vs. engineering compressive strain for the extruded Mg-2%Zn with (a) 0, 0.1, 0.5 and (b) 1, 3, and 5 wt.% Cu additions

double layer at the interface of the electrolyte solution and Mg substrate (Ref 2, 4). According to the fitting results, R_{ct} values decrease as copper addition intensifies. The order from the highest to the lowest values is declared as follows: Mg-2%Zn (160.25 Ω cm^2), Mg-2%Zn-0.1%Cu (101.50 Ω cm^2), Mg-2%Zn-1%Cu (18.20 Ω cm^2), and Mg-2%Zn-5%Cu (5.50 Ω cm^2). This again ascertains that the extruded Mg-2%Zn alloy is the best corrosion-resistant alloy in the present study.

After the accomplishment of polarization tests, corrosion products have been removed with 180 g/L chromic acid, and their SEM images are shown in Fig. 16.

From Fig. 16, surface appearances of the three extruded alloys are characterized by several semi-spherical pits and some areas with the original flat surface, corresponding to the corroded surface and non-corroded surface, respectively. The amount of flat and pit areas is different between the extruded Mg-2%Zn and other Cu-containing alloys. From Fig. 16a, higher amounts of flat areas and also lower pit size can be seen in the Cu-free alloy. Size and depth of pits have also been enlarged for the extruded Mg-2%Zn-0.1%Cu alloy (Fig. 16b). This observation indicates that the corrosion resistance of the extruded Mg-2%Zn-0.1%Cu alloy became worse than that of the extruded Mg-2%Zn alloy. The Mg-2%Zn-5%Cu alloy seems to be corroded at grain boundaries and interior of the grains, as pits abound the surface along with no trace of flat areas (Fig. 16c). All polarization, EIS results, and microstructural observations are in a good agreement, indicating that the corrosion resistance of the extruded Mg-2%Zn-*x*%Cu alloys reduces by adding copper.
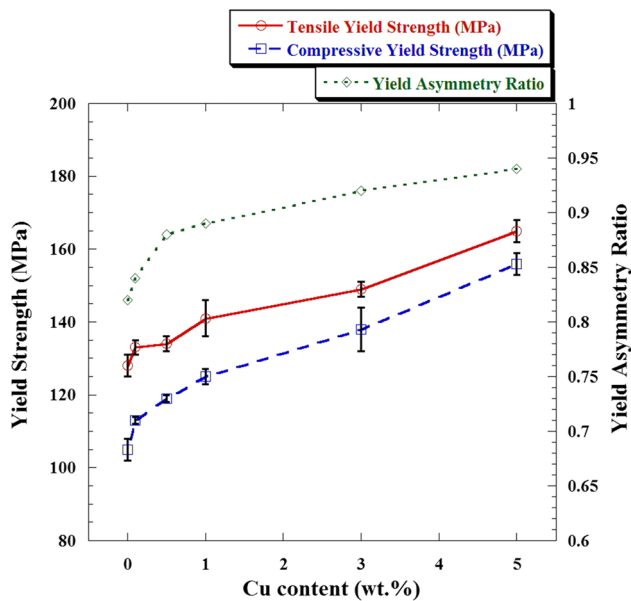
Fig. 13 Tensile and compressive yield strengths (TYS and CYS) and yield asymmetry ratio (YAR) as a function of Cu concentration

It is also interesting to note that corrosion resistance is different for the extruded and cast Mg-Zn alloys. In the as-cast condition of the Mg-1%Zn alloy with the average grain size of 100 μm, two loops have been found in EIS curves, which corresponds to surface film formation (Ref 2). In another research which was about the cast condition of existing alloys, it was found that the Mg-2%Zn alloy had two loops (Ref 10). All of the cast alloys-related diameters were also bigger than the present alloys, which indicates that the corrosion resistance of the cast alloy is higher than that of the extruded alloy (Ref 10). On the other hand, for the extruded Mg-2%Zn alloy with the average grain size of 30 μm, two loops have been discovered in the related EIS curves (Ref 4). However, in this work, the extruded Mg-2%Zn alloy possesses only one loop,

Table 4 Corrosion current density and corrosion potential calculated from polarization curves

| Alloys	E_{corr} (V_{SCE})	I_{corr}, μF/Cm^2
Mg-2%Zn	− 1.49	79.43
Mg-2%Zn-0.1%Cu	− 1.49	50.12
Mg-2%Zn-1%Cu	− 1.45	125.90
Mg-2%Zn-5%Cu	− 1.41	316.23
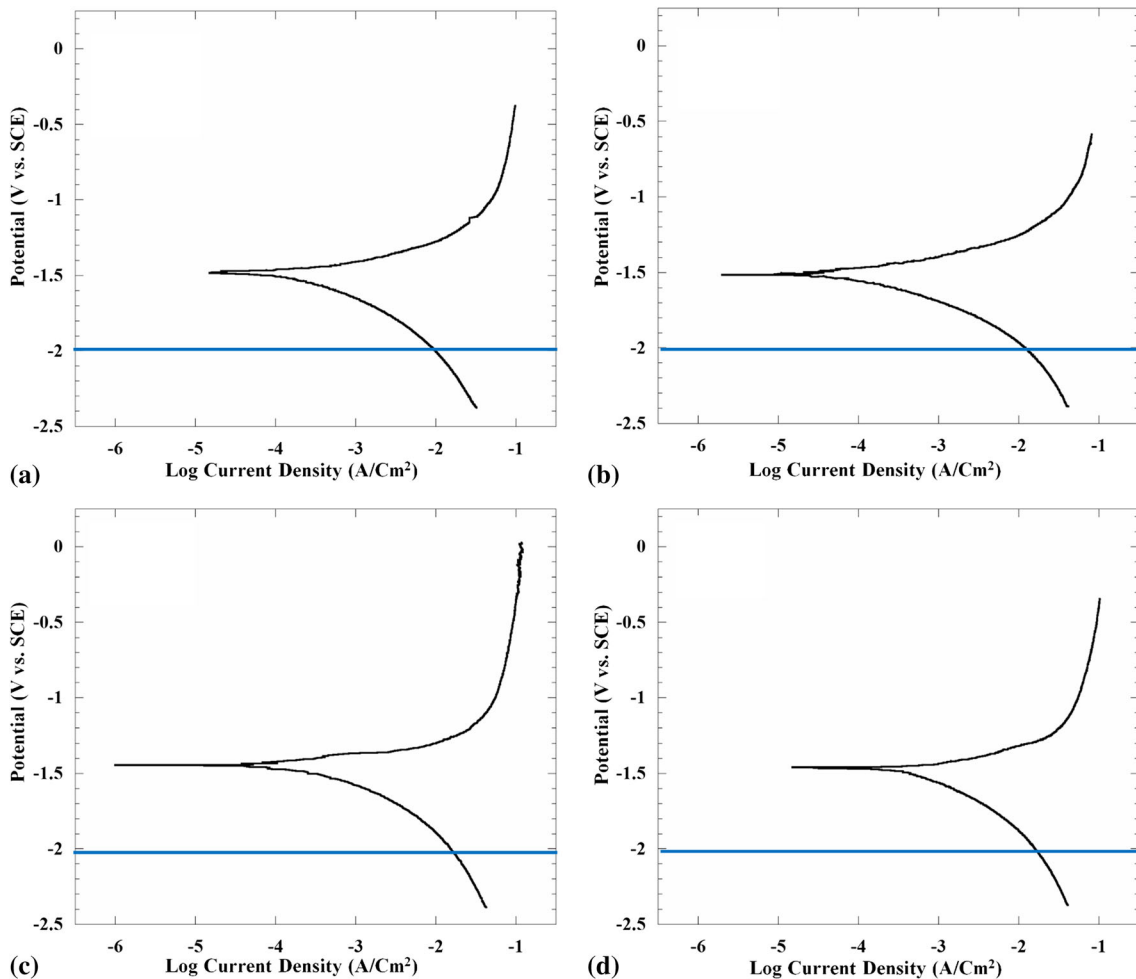
Fig. 14 Polarization curves of the extruded Mg-2%Zn alloy with (a) 0, (b) 0.1, (c) 1 and (d) 5 wt.%Cu additions in 3.5 wt.% NaCl
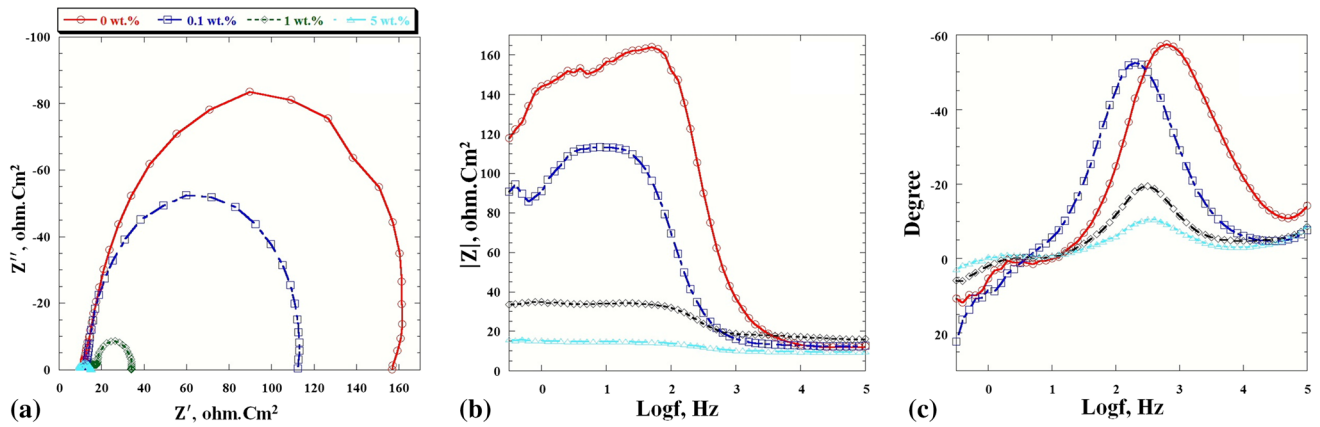
Fig. 15 EIS spectra of the extruded Mg-2%Zn-x%Cu (x = 0, 0.1 and 5 wt.%) alloys in 3.5 wt.% NaCl solution: (a) Nyquist plots; (b) Bode plots of |Z| vs. frequency; and (c) Bode plots of degree vs. frequency

Table 5 Fitting results of the Nyquist plots of the extruded Mg-2%Zn alloys with different additions of copper

Alloys	R_s, Ω cm^2	R_{ct}, Ω cm^2	C, μF cm^{-2}
Mg-2%Zn	13.35 ± 0.28	160.25 ± 15.05	6.29 ± 1.83
Mg-2%Zn-0.1%Cu	12.26 ± 0.97	101.50 ± 8.20	21.58 ± 2.22
Mg-2%Zn-1%Cu	10.83 ± 031	18.20 ± 3.45	40.61 ± 3.87
Mg-2%Zn-5%Cu	9.50 ± 0.30	5.50 ± 1.35	100.03 ± 6.16
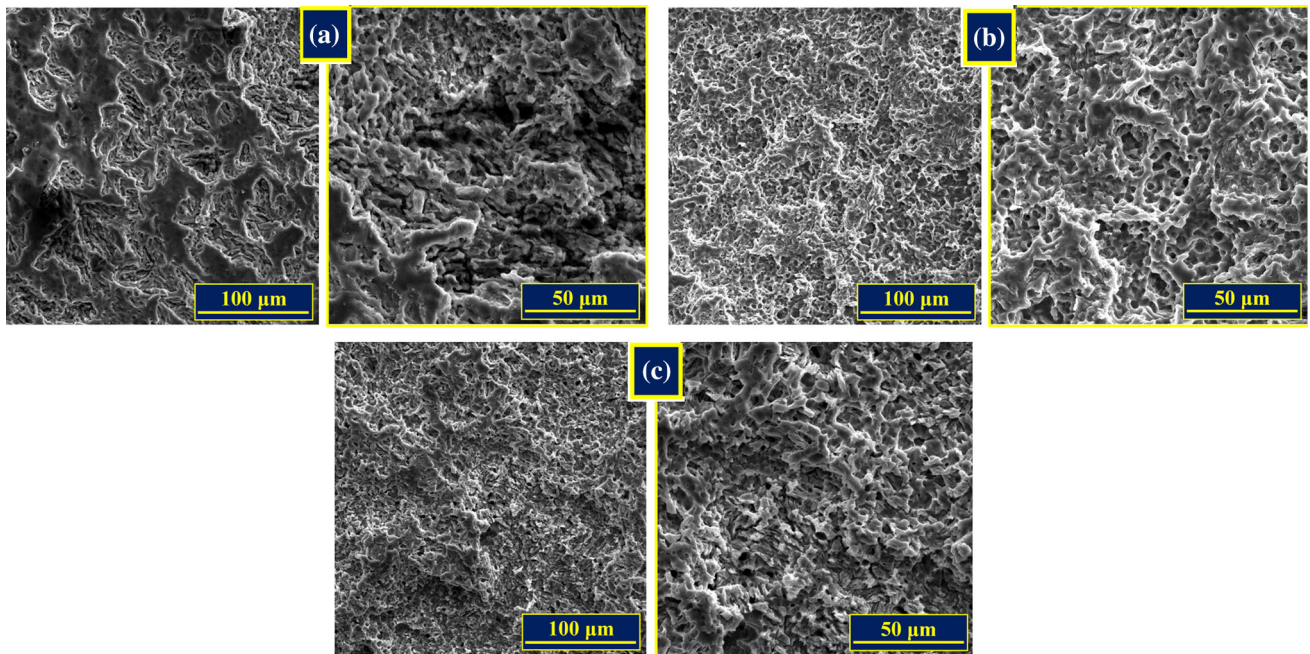
Fig. 16 SEM micrographs of corroded appearance after polarization test and after corrosion product removal for the extruded (a) Mg-2%Zn, (b) Mg-2%Zn-0.1%Cu, (c) Mg-2%Zn-5%Cu alloys

which indicates that the corrosion mechanism is the general dissolution of Mg matrix. According to the microstructural section, the average grain size of the extruded Mg-2%Zn alloy is 13 μm, which is much lower than that of later research studies (Ref 2, 4, 10). As a result, it is apparent that severe mechanical forming results in the presence of more internal tension encouraging more galvanic cells, which also would prevent the formation of the surface film. Generally, the corrosion resistance of the extruded alloys is affected by microstructural features such as grain boundaries, the density of

dislocations and twins, and the distribution and rearrangement of second phases (Ref 44-47). If overall corrosion and Mg dissolution prevail without the formation of a passive layer, grain boundaries surface increment (grain size reduction) and rearrangement of second-phase particles accelerate the corrosion rate. On the other hand, if corrosion depends on passivation, then corrosion rate reduces by those changes (Ref 46, 47). In the current research, no trace of the presence of the passive layer has been seen, so grain boundaries and rearrangement of particles accelerated the corrosion rate.

4. Conclusions

The effects of different amounts of Cu on the microstructure, mechanical, and corrosion properties of the extruded Mg-2%Zn alloy were investigated. The following conclusions were drawn:

(1) By adding 5 wt.% Cu, the average grain size of the extruded Mg-2%Zn alloy was reduced from 13 to 4 μm. The volume percentage of intermetallics was increased from less than 0.1-16% with 5 wt.% Cu addition. According to XRD, SEM, and EDS analysis, the Cu-bearing alloys consisted of Mg_xZn_y, Mg(Zn,Cu), and $Mg(Zn,Cu)_2$ intermetallics.

(2) The Brinell hardness enhanced with Cu addition. The optimum UTS and tensile elongation values were achieved with 0.5 wt.% Cu addition. However, adding 5 wt.% Cu deteriorated the tensile properties, owing to the formation of a high volume fraction of fragile particles acting as crack initiation sites. The TYS and CYS values of the extruded Mg-Zn-Cu alloys increased continuously with more Cu addition. Also, the YAR values improved from 0.82 to 0.94 with 0 wt.% to 5 wt.% Cu, showing the suitable effect of grain size and volume fraction of second-phase particles on the yield asymmetry.

(3) The tensile fracture of the extruded Mg-2%Zn alloy was partly quasi-cleavage, which changed to ductile fracture by adding 0.5 wt.% Cu, due to the existence of more dimples. With higher Cu additions, the fracture mode changed to more brittle, owing to the existence of more cracked particles at the bottom of the dimples.

(4) The corrosion resistance of the extruded alloys decreased with more Cu additions. Excessive addition of Cu over 0.1 wt.% resulted in a high volume fraction of the Mg(Zn,Cu) and $Mg(Zn,Cu)_2$ intermetallics acting as cathodic sites, which encouraged micro-galvanic corrosion acceleration. Moreover, applying the extrusion process was led to the elimination of the oxide layer. Regarding the equal corrosion resistance of the Mg-2%Zn-0.1%Cu alloy with the Mg-2%Zn alloy, and hence its better mechanical properties, the extruded Mg-2%Zn-0.1%Cu alloy was chosen to be the best alloy for further investigation.

References

1. W. Xu, N. Birbilis, G. Sha, Y. Wang, J.E. Daniels, Y. Xiao, and M. Ferry, A High-Specific-Strength and Corrosion-Resistant Magnesium Alloy, *Nat. Mater.*, 2015, **14**, p 1229–1235

2. S. Cai, T. Lei, N. Li, and F. Feng, Effects of Zn on Microstructure, Mechanical Properties and Corrosion Behavior of Mg-Zn Alloys, *Mater. Sci. Eng. C*, 2012, **32**, p 2570–2577

3. S. Zhang, X. Zhang, C. Zhao, J. Li, Y. Song, C. Xie, H. Tao, Y. Zhang, Y. He, Y. Jiang, and Y. Bian, Research on an Mg-Zn Alloy as a Degradable Biomaterial, *Acta Biomater.*, 2010, **6**, p 626–640

4. Y. Song, E.H. Han, D. Shan, C.D. Yim, and B.S. You, The Effect of Zn Concentration on the Corrosion Behavior of Mg-x%Zn Alloys, *Corros. Sci.*, 2012, **65**, p 322–330

5. C.J. Boehlert and K. Knittel, The Microstructure, Tensile Properties, and Creep Behavior of Mg-Zn Alloys Containing 0-4.4 wt.% Zn, *Mater. Sci. Eng. A*, 2006, **417**, p 315–321

6. A. Srinivasan, Y. Huang, C.L. Mendis, C. Blawert, K.U. Kainer, and N. Hort, Investigations on Microstructures, Mechanical and Corrosion Properties of Mg-Gd-Zn alloys, *Mater. Sci. Eng. A*, 2014, **595**, p 224–234

7. Y. Song, E.H. Han, D. Shan, C.D. Yim, and B.S. You, The Role of Second Phases in the Corrosion Behavior of Mg-5Zn Alloy, *Corros. Sci.*, 2012, **60**, p 238–245

8. Y. Lu, R. Bradshaw, Y.L. Chiu, and I.P. Jones, The Role of Precipitates in the Bio-corrosion Performance of Mg-3Zn in Simulated body Fluid, *J. Alloys. Compd.*, 2014, **614**, p 345–352

9. Y. Yan, H. Cao, Y. Kang, K. Yu, T. Xiao, J. Luo, Y. Deng, H. Fang, H. Xiong, and Y. Dai, Effects of Zn Concentration and Heat Treatment on the Microstructure, Mechanical Properties and Corrosion Behavior of As-Extruded Mg-Zn Alloys Produced by Powder Metallurgy, *J. Alloys Compd.*, 2017, **693**, p 1277–1289

10. L. Liu, X. Chen, F. Pan, Z. Wang, W. Liu, P. Cao, T. Yan, and X. Xu, Effect of Y and Ce Additions on Microstructure and Mechanical Properties of Mg-Zn-Zr Alloys, *Mater. Sci. Eng. A*, 2015, **644**, p 247–253

11. Y. Du, M. Zheng, X. Qiao, D. Wang, W. Peng, K. Wu, and B. Jiang, Improving Microstructure and Mechanical Properties in Mg-6 mass% Zn Alloys by Combined Addition of Ca and Ce, *Mater. Sci. Eng. A*, 2016, **656**, p 67–74

12. T. Bhattacharjee, T. Nakata, T.T. Sasaki, S. Kamado, and K. Hono, Effect of Microalloyed Zr on the Extruded Microstructure of Mg-6.2Zn-Based Alloys, *Scr. Mater.*, 2014, **90-91**, p 37–40

13. M. Lotfpour, M. Emamy, C. Dehghanian, and K. Tavighi, Influence of Cu Addition on the Structure, Mechanical and Corrosion Properties of Cast Mg-2%Zn Alloy, *J. Mater. Eng. Perform.*, 2017, **26**, p 2136–2150

14. S. Zhu, T. Luo, T. Zhang, Y. Li, and Y. Yang, Effects of Cu Addition on the Microstructure and Mechanical Properties of As-Cast and Heat Treated Mg-6%Zn-4%Al Magnesium Alloy, *Mater. Sci. Eng. A*, 2017, **689**, p 203–211

15. C. Dehghanian, M. Lotfpour, and M. Emamy, The Microstructure, and Mechanical and Corrosion Properties of As-Cast and As-Extruded Mg-2%Zn-x%Cu Alloys After Solution and Aging Heat Treatments, *J. Mater. Eng. Perform.*, 2019, **28**, p 2305–2315

16. H.M. Zhu, C.P. Luo, J.W. Liu, and D.L. Jiao, Growth Twinning Behavior of Cast Mg-Zn-Cu-Zr Alloys, *Trans. Nonferrous Met. Soc.*, 2014, **24**, p 316–320

17. J. Buha and T. Ohkubo, Natural Aging in Mg-Zn (-Cu) Alloys, *Metall. Mater. Trans. A*, 2008, **39**, p 2259

18. H.M. Zhu, G. Sha, J.W. Liu, C.L. Wu, C.P. Luo, Z.W. Liu, R.K. Zheng, and S.P. Ringer, Microstructure and Mechanical Properties of Mg-6Zn-xCu-0.6Zr (wt%) Alloys, *J. Alloys Compd.*, 2011, **509**, p 3526–3531

19. H.M. Zhu, C.P. Luo, J.W. Liu, and D.L. Jiao, Effects of Cu Addition on Microstructure and Mechanical Properties of As-Cast Magnesium Alloy ZK60, *Trans. Nonferrous Met. Soc.*, 2014, **24**, p 605–610

20. X. Chen, L. Liu, F. Pan, J. Mao, X. Xu, and T. Yan, Microstructure, Electromagnetic Shielding Effectiveness and Mechanical Properties of Mg-Zn-Cu-Zr Alloys, *Mater. Sci. Eng. B*, 2015, **197**, p 67–74

21. S. Golmakaniyoon and R. Mahmudi, Comparison of the Effects of La- and Ce-Rich Rare Earth Additions on the Microstructure, Creep Resistance, and High-Temperature Mechanical Properties of Mg-6Zn-3Cu Cast Alloy, *Mater. Sci. Eng. A*, 2011, **528**, p 5228–5233

22. J.H. Jun, J.M. Kim, B.K. Park, K.T. Kim, and W.J. Jung, Effects of Rare Earth Elements on Microstructure and High Temperature Mechanical Properties of ZC63 Alloy, *J. Mater. Sci.*, 2005, **40**, p 2659–2661

23. E.A. Ball and P.B. Prangnell, Tensile-Compressive Yield Asymmetries in High Strength Wrought Magnesium Alloys, *Scr. Mater.*, 1994, **31**, p 111–116

24. F.J. Humphreys and M. Hatherly, *Recrystallization and Related Annealing Phenomena*, 2nd ed., Pergamon Press, Oxford, 2004, p 285–319

25. C.J. Wang, K.K. Deng, K.B. Nie, S.J. Shang, and W. Liang, Competition Behavior of the Strengthening Effects in As-Extruded AZ91 Matrix: Influence of Pre-existed $Mg_{17}Al_{12}$ Phase, *Mater. Sci. Eng. A*, 2016, **656**, p 102–110

26. C.A. Nijnez-lopez, P. Skeldon, G.E. Thompson, P. Lyon, H. Karimzadeh, and T.E. Wilks, The Corrosion Behaviour of Mg Alloy ZC71/SiCp Metal Matrix Composite, *Corros. Sci.*, 1995, **37**, p 689–708

27. R. Xu, M.C. Zhao, Y.C. Zhao, L. Liu, C. Liu, C. Gao, C. Shuai, and A. Atrens, Improved Biodegradation Resistance by Grain Refinement of Novel Antibacterial ZK30-Cu Alloys Produced via Selective Laser Melting, *Mater. Lett.*, 2019, **237**, p 253–257

28. S.-M. Baek, B. Kim, and S.S. Park, Influence of Intermetallic Particles on the Corrosion Properties of Extruded ZK60 Mg Alloy Containing Cu, *Metals*, 2018, **8**, p 323

29. C. Shuaia, L. Liu, M. Zhao, P. Feng, Y. Yang, W. Guo, C. Gao, and F. Yuan, Microstructure, Biodegradation, Antibacterial and Mechanical Properties of ZK60-Cu Alloys Prepared by Selective Laser Melting Technique, *J. Mater. Sci. Technol.*, 2018, **34**(10), p 1944–1952

30. C. Liu, X. Fu, H. Pan, P. Wan, L. Wang, L. Tan, K. Wang, Y. Zhao, K. Yang, and P.K. Chu, Biodegradable Mg-Cu Alloys with Enhanced Osteogenesis, Angiogenesis, and Long-Lasting Antibacterial Effects, *Sci. Rep.*, 2016, **6**, p 27374

31. X. Yan, P. Wan, L. Tan, M. Zhao, L. Qin, and K. Yang, Corrosion and Biological Performance of Biodegradable Magnesium Alloys Mediated by Low Copper Addition and Processing, *Mater. Sci. Eng. A*, 2018, **93**, p 565–581

32. X. Yan, P. Wan, L. Tan, M. Zhao, C. Shuai, and K. Yang, Influence of Hybrid Extrusion and Solution Treatment on the Microstructure and Degradation Behavior of Mg-0.1Cu Alloy, *Mater. Sci. Eng. A*, 2018, **229**, p 105–117

33. J.D. Robson, D.T. Henry, and B. Davis, Particle Effects on Recrystallization in Magnesium-Manganese Alloys: Particle-Stimulated Nucleation, *Acta Mater.*, 2009, **57**, p 2739–2747

34. H. Okamoto, Comment on Mg-Zn (Magnesium-Zinc), *Phase Equilib. Diffus.*, 1994, **15**, p 129–130

35. W. Chen and J. Sun, The Electronic Structure and Mechanical Properties of $MgCu_2$ Laves Phase Compound, *Physica B*, 2006, **382**, p 279–284

36. B. Kim, S.M. Baek, H.Y. Jeong, J.G. Lee, and S.S. Park, Grain refinement and Reduced Yield Asymmetry of Extruded Mg-5Sn-1Zn Alloy by Al Addition, *J. Alloys Compd.*, 2016, **660**, p 304–309

37. N.J. Petch, The Cleavage Strength of Polycrystals, *J. Iron Steel Inst.*, 1953, **174**, p 25

38. E.O. Hall, The Deformation and Ageing of Mild Steel: II, Characteristics of the Lüders Deformation, *Proc. Phys. Soc. B.*, 1951, **64**, p 747

39. G. Mima and Y. Tanaka, Grain Size Dependence of Yield Stress and Flow Stress in the Age-Hardened Magnesium-Zinc Alloy, *Trans JIM*, 1971, **12**, p 317

40. M.R. Barnett, Z. Keshavarz, A.G. Beer, and D. Atwell, Influence of Grain Size on the Compressive Deformation of Wrought Mg-3Al-1Zn, *Acta Mater.*, 2004, **52**, p 5093–5103

41. Y. Jiang, Y. Chen, and G. Gao, Role of Volume Fraction of Second Phase Particles, Dislocation-Twin and Twin–Twin Interactions in the Reduced Tension-Compression Yield Asymmetry, *Mater. Des.*, 2016, **97**, p 131–137

42. S.M. Yin, C.H. Wang, Y.D. Diao, S.D. Wu, and S.X. Li, Influence of Grain Size and Texture on the Yield Asymmetry of Mg-3Al-1Zn Alloy, *J. Mater. Sci. Technol.*, 2011, **27**, p 29–34

43. J. Jain, W.J. Poole, C.W. Sinclair, and M.A. Gharghouri, Reducing the Tension-Compression Yield Asymmetry in a Mg-8Al-0.5Zn Alloy via Precipitation, *Scr. Mater.*, 2010, **62**, p 301–304

44. M. Ben-Haroush, G. Ben-Hamu, D. Eliezer, and L. Wagner, The Relation Between Microstructure and Corrosion Behavior of AZ80 Mg Alloy Following Different Extrusion Temperatures, *Corros. Sci.*, 2008, **50**, p 1766–1778

45. G.L. Song and Z.Q. Xu, The Surface, Microstructure and Corrosion of Magnesium Alloy AZ31 Sheet, *Electrochim. Acta*, 2010, **55**, p 4148–4161

46. T. Zhang, Y. Shao, G. Meng, Z. Cui, and F. Wang, Corrosion of Hot Extrusion AZ91 Magnesium Alloy: I-Relation Between the Microstructure and Corrosion Behavior, *Corros. Sci.*, 2011, **53**, p 1960–1968

47. N.N. Aung and W. Zhou, Effect of Grain Size and Twins on Corrosion Behaviour of AZ31B Magnesium Alloy, *Corros. Sci.*, 2010, **52**, p 589–594